


High-temperature transport in the one-dimensional mass-imbalanced Fermi-Hubbard modelThomas G. Kiely  and Erich J. Mueller *Department of Physics, Cornell University, Ithaca, New York 14853, USA* (Received 11 April 2024; accepted 30 May 2024; published 12 June 2024)

We study transport in the one-dimensional mass-imbalanced Fermi-Hubbard model in the high-temperature limit, focusing on the case of strong interactions. Prior theoretical and experimental investigations have revealed unconventionally long transport timescales, with complications due to strong finite-size effects. We compute the dynamical current-current correlation function directly in the thermodynamic limit using infinite tensor network techniques. We show that transport in the strong-imbalance limit is dominated by AC resonances, which we compute with an analytic expansion. We study the dephasing of these resonances with mass imbalance, η . In the small-imbalance limit, the model is nearly integrable. We connect these unusual limits by computing the DC conductivity and transport decay time as a function of η and the interaction strength U/t . We propose an experimental protocol to measure these correlation functions in cold atom experiments.

DOI: [10.1103/PhysRevA.109.063318](https://doi.org/10.1103/PhysRevA.109.063318)**I. INTRODUCTION**

The one-dimensional (1D) mass-imbalanced Fermi-Hubbard model, where \uparrow -spin particles hop more easily than \downarrow spins, interpolates between two interesting limits. When the masses are equal the system is integrable. When the mass ratio diverges the heavy particles act as stationary disorder, localizing the light particles. In neither of these limits does the system have typical metallic behavior. Between them the system is nonintegrable and should display conventional metallic behavior, but it is challenging to calculate the conductivity when the interactions are strong. In this paper we use infinite tensor network methods and analytic expansions to study the high-temperature optical conductivity of this model.

In a conventional (nonintegrable) metallic system, the zero-temperature charge conductivity exhibits a zero-frequency δ -function peak whose area is the Drude weight [1]. At any temperature $T > 0$, scattering processes broaden this peak, and the Drude weight vanishes. Instead, the conductivity at frequency ω has the approximate Drude form $\sigma(\omega) = \sigma_{\text{DC}}/(1 - i\omega\tau)$ with a transport scattering time τ , and DC conductivity σ_{DC} . Integrable systems are characterized by an infinite number of conserved quantities, and consequently violate this simple picture [2]. For example, the ordinary (mass-balanced) 1D Fermi-Hubbard model exhibits a finite Drude weight at *all* temperatures so long as the total charge density \bar{n} is not unity [3]. This feature corresponds to an infinite DC conductivity, which in higher dimensions is only seen in superfluids or zero-temperature metals. At half filling ($\bar{n} = 1$), the Drude weight vanishes but the high-temperature transport is still unconventional, displaying a Kardar-Parisi-Zhang (KPZ) dynamical scaling [4–8] which has recently been attributed to a non-Abelian SO(4) symmetry [9].

The limit of strong mass imbalance also displays unusual transport. When the heavy-particle hopping vanishes, local heavy-particle densities are constants of motion, and hence the system is integrable. This integrable limit has vastly different

properties than the symmetric-mass limit. The static heavy particles act as disorder, leading to Anderson localization of the light particles [10]. In one dimension this localization occurs for any nonzero interaction strength. In a compelling but incorrect argument, it was proposed that analogous physics might be found if the heavy particles were allowed to hop, leading to many-body localization in a translationally invariant system [11–13]. Subsequent work, however, provided evidence that the model is ergodic for any finite mass ratio and interaction strength [14–17]. Nonetheless, the system displays “anomalously long” decay times [18,19], and there is a timescale over which the behavior appears nondiffusive. One essential feature is that the long-time limit ($\tau \rightarrow \infty$) does not commute with the thermodynamic limit ($L \rightarrow \infty$), and results from finite-size numerics are only reliable for short times. In our numerical calculations, we leverage tensor network techniques to study transport properties directly in the thermodynamic limit, circumventing this challenge.

Ultracold atom experiments have recently realized the mass-imbalanced Fermi Hubbard model [20]. Fermionic ytterbium atoms are trapped in a two-dimensional (2D) near-resonant optical lattice. Due to the spin-dependent AC polarizability, atoms with different internal states see lattices of different depths, and hence have different effective masses [21]. The mass ratio depends on the frequency of the lattice lasers and approaches unity for a far-detuned lattice. Such state-dependent lattices have also been realized using fermionic strontium [22] and potassium [23] atoms as well as bosonic rubidium [24]. Interactions are tuned by a Feshbach resonance [25,26]. In these experiments, conventional transport observables (e.g., DC resistivity) are not easily accessible. Instead, transport is studied by introducing spin or charge deformations and observing their relaxation [20,27–30]. We propose and model a technique to extract the current-current correlation function from the dynamical response to a probe.

In Sec. II, we introduce the mass-imbalanced Fermi-Hubbard model and discuss the transport properties studied

here. In Sec. III, we present our numerical results. In Sec. IV we perform an analytic expansion about the large-mass-ratio and strong-interaction limit, which is shown to quantitatively model the transport properties. In Sec. V we discuss experimental implications of our work, including a proposal for measuring the current-current correlation function in ultracold atomic systems. Our conclusions are presented in Sec. VI.

II. FORMALISM

A. Fermi-Hubbard model

The mass-imbalanced Fermi-Hubbard model is defined by the Hamiltonian

$$H = - \sum_{i\mu} (t_\mu c_{i,\mu}^\dagger c_{i+1,\mu} + \text{H.c.}) + U \sum_i n_{i,\uparrow} n_{i,\downarrow}, \quad (1)$$

where i labels the sites, $\mu = \uparrow, \downarrow$ labels the spins, and t_μ and U parametrize the kinetic and interaction energies, respectively. We also write $t_\uparrow = t$ and $t_\downarrow = \eta t$, so that η parametrizes the mass imbalance. We take $0 \leq \eta \leq 1$, defining \downarrow spins as the heavy particles.

As already explained, in the absence of any mass imbalance ($\eta = 1$), the model is integrable and can be solved exactly with the Bethe ansatz [31,32]. Adding a mass imbalance ($\eta < 1$) formally breaks integrability.

In the limit of infinite mass imbalance ($\eta = 0$), Eq. (1) reduces to the Falicov-Kimball model [33], which has an extensive number of local conserved densities: $[H, n_{i,\downarrow}] = 0 \forall i$. One can think of the model as describing noninteracting spinless fermions interacting with a static binary potential given by the configuration of heavy spins. At high temperatures the thermal density matrix sums over all possible binary disorder configurations, and the model is expected to exhibit Anderson localization for $\eta = 0$ [18,34]. For finite $\eta \rightarrow 0$, the model is ergodic but with a diverging relaxation time [14–17,19].

We report on the case of *half filling* where the ensemble-average number of particles on a site are $\langle n_{i\mu} \rangle = 1/2$. In the $\eta = 1$ model, the half filled system has an enhanced symmetry with respect to other fillings, resulting in unconventional subdiffusive dynamical scaling [9]. This makes the half filled case particularly interesting. At other fillings, transport is ballistic when $\eta = 1$ [3]. For generic $\eta \neq 1$, we expect that results at different densities are qualitatively similar.

B. Transport

In this paper we quantify transport by studying the behavior of the optical conductivity. Using the fluctuation-dissipation theorem [35], one can express the real part of the spin- and site-resolved conductivity as

$$\sigma_{\mu\nu}(l, m; \omega) = \frac{1 - e^{-\beta\omega}}{2\omega} \int_{-\infty}^{\infty} d\tau e^{i\omega\tau} \Lambda_{\mu\nu}(l, m; \tau), \quad (2)$$

where $\Lambda_{\mu\nu}(i, j; \tau)$ is the current-current correlation function:

$$\Lambda_{\mu\nu}(l, m; \tau) = \text{Tr}(e^{-\beta H} j_\mu(l, \tau) j_\nu(m, 0)). \quad (3)$$

The current operator acting on sites $(l, l+1)$ is defined as

$$j_\mu(l) = -it_\mu (c_{l+1,\mu}^\dagger c_{l,\mu} - \text{H.c.}), \quad (4)$$

and $j_\mu(l, \tau) = e^{iH\tau} j_\mu(l) e^{-iH\tau}$. Of course, the conventional expression for the optical conductivity is recovered by summing over indices l and m :

$$\sigma(\omega) = \frac{1}{N} \sum_{l,m} \sigma(l, m; \omega). \quad (5)$$

We will mainly be concerned with $\sigma = \sigma_{\uparrow\uparrow}$, and for notational simplicity will denote $j = j_\uparrow$, and $\Lambda = \Lambda_{\uparrow\uparrow}$, omitting the subscripts when we are referring to the light particles. We make this choice because the high-temperature charge (σ_c) and spin (σ_s) conductivities are both directly proportional to $\sigma_{\uparrow\uparrow}$ when $\eta = 0$ and $\eta = 1$.

For systems with a bounded spectrum, as we consider here, we can expand Eq. (2) in the high-temperature limit, $T \gg t, U$ [36–39]:

$$\sigma(l, m; \omega) = \frac{\beta}{2} \int_{-\infty}^{\infty} d\tau e^{i\omega\tau} \text{Tr}(j(l, \tau) j(m, 0)) + \dots \quad (6)$$

Thus, up to an overall factor of β , the high-temperature optical conductivity is simply the Fourier transform of the current-current correlation function, $\Lambda(l, m; \tau) = \text{Tr}(j(l, \tau) j(m, 0))$. This expansion can be performed for $\sigma_{\uparrow\uparrow}$ and $\sigma_{\downarrow\downarrow}$, but the cross terms, $\sigma_{\uparrow\downarrow}$, are only nonzero at second order ($\propto \beta^2$). Here we focus on the leading-order expansion, studying $\Lambda(\tau)$.

Going forward, we present calculations performed on uniform, infinite-temperature systems in the thermodynamic limit. Making use of translational invariance, we define $\Lambda(x, \tau) = (1/N) \sum_l \Lambda(l, l+x; \tau)$, which is well defined in the limit $N \rightarrow \infty$. In one dimension, the units of the current-current correlation function are those of a squared characteristic rate, and hence we report it in units of t^2 . We report values for the high-temperature conductivity in units of $\sigma_{\text{ref}} = a\beta t$, where a is the lattice spacing. This corresponds to the conductivity from a random diffusive walk with scattering time $1/t$ and a mean-free path a .

C. Tensor network techniques

We compute the real-time, spatially resolved current-current correlation function $\Lambda(x, \tau)$ at infinite temperature using infinite tensor network techniques [40,41]. As described in Appendix A 1, we purify the infinite-temperature density matrix, writing it as $\rho_0 = \text{Tr}|\psi_0\rangle\langle\psi_0|$ where the trace is taken over a set of auxiliary degrees of freedom, corresponding to a copy of the original system [40,41]. We write $|\psi_0\rangle$ as an infinite matrix product state.

Operator expectation values can be written as $\text{Tr}(\rho_0 \hat{O}) = \langle\psi_0|\hat{O}_{\text{phys}}|\psi_0\rangle$ where \hat{O}_{phys} acts only on the physical degrees of freedom of $|\psi_0\rangle$. Given this definition, we may write the current-current correlation function as an expectation value:

$$\Lambda(x, \tau) = \langle\psi_0|e^{iH_{\text{phys}}\tau} j_{\text{phys}}(0) e^{-iH_{\text{phys}}\tau} j_{\text{phys}}(x)|\psi_0\rangle, \quad (7)$$

where $j_{\text{phys}}(0)$ is a local current operator of the form in Eq. (4) connecting the *physical* sites at $x = 0$ and $x = 1$. As the infinite-temperature density matrix is simply the identity operator, its purification has a special property: for any operator \hat{O}_{phys} acting on the physical degrees of freedom, there is a unique operator \hat{O}'_{aux} acting only on the auxiliary degrees of freedom which satisfies $\hat{O}_{\text{phys}}|\psi_0\rangle = \hat{O}'_{\text{aux}}|\psi_0\rangle$ [42]. The

relationship between \hat{O} and \hat{O}' is determined by the choice of purification, $|\psi_0\rangle$, which is not unique. In Appendix A 1 we elaborate on how the choice of purification can be useful in implementing block-sparsity constraints [43], and we show how to determine the auxiliary partner \hat{O}' to an operator \hat{O} for a given purification.

Given this property of $|\psi_0\rangle$, we define H'_{aux} as the auxiliary partner of the Hamiltonian, H_{phys} . This allows us to rewrite Eq. (7) as

$$\Lambda(x, \tau) = \langle \psi_0 | j_{\text{phys}}(0) e^{-i(H_{\text{phys}} - H'_{\text{aux}})\tau} j_{\text{phys}}(x) | \psi_0 \rangle, \quad (8)$$

where we have taken advantage of the fact that operators acting on the auxiliary and physical degrees of freedom commute with one another. The exponentiated object $H_{\text{phys}} - H'_{\text{aux}}$ is effectively the Liouvillian superoperator \mathcal{L} , which conventionally is defined by its action on an operator \hat{O} : $\mathcal{L}\hat{O} = [H, \hat{O}]$ [36]. Indeed,

$$(H_{\text{phys}} - H'_{\text{aux}})\hat{O}_{\text{phys}}|\psi_0\rangle = ([H, \hat{O}])_{\text{phys}}|\psi_0\rangle. \quad (9)$$

To compute a spatially dependent correlation function $\Lambda(x, \tau)$ without finite-size effects, we allow a ‘‘window’’ within an infinite matrix product state (MPS) to evolve nonuniformly. As the window is time-evolved, the region of nonuniformity will be housed within a light-cone that expands linearly in time, at least for short times. To accommodate this, we allow the system to add un-evolved sites to the boundaries, creating a dynamically expanding window [44–46]. So long as the threshold for adding sites is set sufficiently low, there will be effectively no finite-size dependence. While the present analysis will focus on uniform properties (corresponding to the Fourier $k = 0$ component), we show features of our site-resolved technique in Appendix A 4.

To time-evolve the MPS, we sequentially multiply $|\psi_0\rangle$ by the W^{II} approximation to the time-evolution operator [41,47], truncating the bond dimension at each step. We utilize a third-order split-step method [41,47] and choose a time step $\Delta\tau = 0.01/t$. With these short time steps our method is extremely accurate. Unlike some alternative techniques, there are no challenges here with dynamically expanding the bond dimension [48]. The results shown here use maximum bond dimensions of $\chi = 750\text{--}1000$. We emphasize that, for the times shown, our MPS simulations are numerically exact.

III. RESULTS

A. High-frequency properties

In Fig. 1(a) we show the uniform current-current correlator in the temporal domain, $\Lambda(\tau) = \sum_x \Lambda(x, \tau)$, for $U/t = 20$ and a series of mass ratios $\eta = 0, 0.1, 0.2, 0.3, 0.4, 0.5$. For small η , the correlation function is dominated at short times by large oscillations at a frequency $\omega \sim U$, and slower oscillations with $\omega \sim t$. The rapid oscillations have an envelope which is modulated at a lower frequency $\omega \sim t$. Note that $\Lambda(0) = t^2/2$ is constrained by a sum rule and is independent of η .

For infinite mass imbalances ($\eta = 0$), each of these oscillatory components persists indefinitely. This can be understood by recognizing that the Falicov-Kimball model is an exactly solvable model of free fermions in a binary-disordered

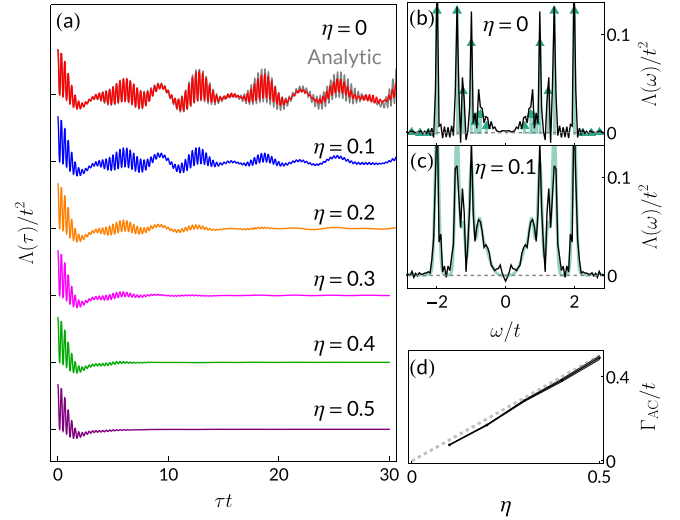


FIG. 1. (a) Uniform current-current correlation function, $\Lambda(\tau) = \sum_x \Lambda(x, \tau)$, for $U/t = 20$ and a variety of mass ratios. Curves are offset for visual clarity. Tick marks denote the zero value at each η , and in all cases $\Lambda(0) = t^2/2$. For $\eta = 0$, there are persistent oscillations out to long times. Our analytic model, derived in the limit $\eta, t/U \rightarrow 0$, is shown in gray behind the $\eta = 0$ data—we capture the period of oscillations and their amplitude modulations very accurately. Deviations are due to nonzero t/U . For $\eta > 0$, these oscillations are damped by the motion of heavy particles. (b), (c) We can extract the damping rate for a given η by fitting the Fourier transform of $\Lambda(\tau)$ to the analytic result with a Gaussian broadening factor (see main text). Panel (b) shows the precise agreement for $\eta = 0$, without broadening, and panel (c) shows the agreement at $\eta = 0.1$. (d) Fitted Gaussian broadening factor, Γ_{AC} , as a function of η . Dashed line is $\Gamma_{\text{AC}} = \eta$, which appears to describe the data very well.

background potential. In one dimension, this system is Anderson-localized for arbitrarily small U/t , so $\sigma(\omega = 0) = 0$. For large U/t , the light-particle wave functions are all localized to regions of constant background potential (i.e., regions in which $\langle n_{\downarrow} \rangle = 0$ or 1 throughout). When we take the thermal ensemble average, the properties of the system can be written as a sum of contributions from disjoint regions, each of which possess a quantized energy spectrum. Consequently, the Fourier transform of the current-current correlator, $\Lambda(\omega)$, is a discrete sum over δ functions. In Appendix C, we carry out an analytic calculation of $\Lambda(\tau)$ when the single-particle wave functions are completely localized, i.e., the limit $\eta, t/U \rightarrow 0$. The resulting time series is plotted as the gray curve in Fig. 1(a), sitting behind the $\eta = 0$ data, which closely matches the numerical results out past 10 tunneling times. Deviations from the analytic expression are due to the finite localization length at $U/t = 20$.

As shown in Fig. 1, the long-lived oscillations at $\eta = 0$ are damped for finite η . In the frequency domain, we find that the finite η spectra are well approximated by Gaussian broadening our analytic $\eta = 0$ results. Figure 1(b) shows the Fourier transform of the $\eta = 0$ data from Fig. 1(a). The resulting peaks are well-aligned with the locations of the δ functions in our analytic theory, shown with colored triangles. Figure 1(c) shows the spectrum for $\eta = 0.1$. Colored lines

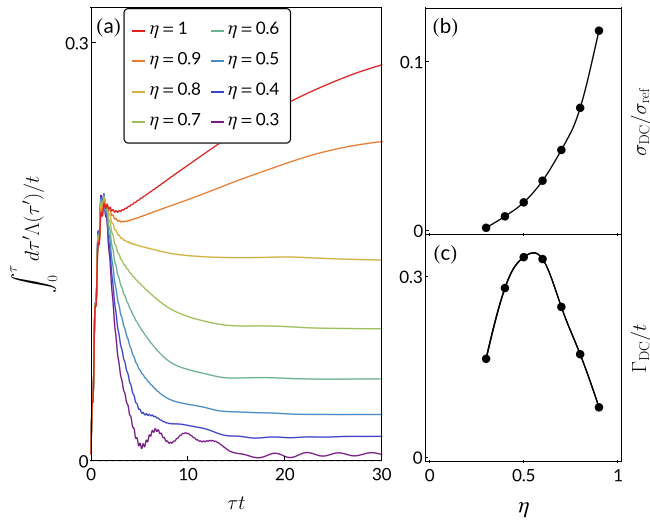


FIG. 2. (a) Integral of the uniform current-current correlation function, $\int_0^\tau d\tau' \Lambda(\tau')$, for $U/t = 20$ and a variety of mass ratios. Integrating the time series reduces the contributions from rapidly oscillating terms, allowing one to more easily extract the low-frequency behavior. For $\eta = 0.3$, oscillations with $\omega \sim t$ have a substantial amplitude even out to 30 tunneling times; these oscillations are even larger for $\eta < 0.3$, so those curves have been omitted for visual clarity. Fitting the long-time behavior of these curves to the form $T\sigma_{DC}/2 + Ce^{-\Gamma_{DC}\tau}$, we can extract the DC conductivity, σ_{DC} and the DC transport relaxation rate, Γ_{DC} . These are shown as a function of η in panels (b) and (c), respectively. We find that σ_{DC} appears to vanish continuously as $\eta \rightarrow 0$ and diverges as $\eta \rightarrow 1$. The transport relaxation rate exhibits nonmonotonic behavior, peaking around $\eta = 0.5$ and vanishing at $\eta = 0, 1$. These features are consistent with the fact that both the $\eta = 0$ and $\eta = 1$ limits are integrable.

depict our analytic $\eta = 0$ result, broadened by a Gaussian of width $\Gamma_{AC}/t = 0.077$. For each value of η , we find the best fit Γ_{AC} . As shown in Fig. 1(d), Γ_{AC} is proportional to η with a proportionality constant close to 1 (gray dashed line). This provides a strong indication that the principle damping mechanism is the motion of heavy particles, which should occur on timescales $\sim 1/\eta t$, hence resulting in $\Gamma_{AC} \propto \eta$. While this AC damping rate is not a common transport coefficient to measure in condensed-matter systems, cold atom experiments are well-placed to extract it by studying the envelope of $\omega \sim U$ oscillations in the current-current correlation functions (see Sec. V).

B. Low-frequency properties

In Fig. 2(a) we show the integrated uniform current-current correlator, $\int_0^\tau d\tau' \Lambda(\tau')$, for a variety of mass ratios. This quantity is convenient for studying the low-frequency properties of $\Lambda(\tau)$, as contributions from components oscillating with frequency ω will generically be diminished by a factor of $1/\omega^2$. For small η , however, these components are nonetheless substantial, and hence those curves are omitted from Fig. 2 for clarity.

After a short-time increase, the integrated time series for intermediate values of η slowly relax to a constant value at long times. Up to prefactors, this asymptotic value is

the DC conductivity: $\lim_{\tau \rightarrow \infty} \int_0^\tau d\tau' \Lambda(\tau')/t = 2\sigma_{DC}/\sigma_{ref}$ [cf. Eq. (6)]. As introduced in Sec. II, $\sigma_{ref} = a\beta t$, where a is the lattice spacing, β the inverse temperature, and t the hopping matrix element. We extract the asymptotic conductivity, σ_{DC} as well as the transport relaxation rate, Γ_{DC} , by fitting the integrated time series to the form $\int_0^\tau d\tau' \Lambda(\tau')/t = 2\sigma_{DC}/\sigma_{ref} + Ce^{-\Gamma_{DC}\tau}$ with $\{C, \sigma_{DC}, \Gamma_{DC}\}$ as fitting parameters. Fitting was performed for $\tau \geq 6/t$. These two DC transport properties are shown as functions of η in Figs. 2(b) and 2(c), respectively.

We find that the DC conductivity diverges continuously as $\eta \rightarrow 1$, while the relaxation rate vanishes. This divergence is consistent with superdiffusive behavior at $\eta = 1$. Superdiffusivity is characterized by a dynamical exponent $1 < z < 2$, which describes the long-time hydrodynamic relationship between spatial and temporal fluctuations; diffusive transport corresponds to $z = 2$, while ballistic transport corresponds to $z = 1$. For the half-filled 1D Hubbard model one expects KPZ dynamical scaling, corresponding to a dynamical exponent $z = 3/2$ [9]. As described in Appendix B, the dynamical exponent is directly related to the long-time behavior of the integrated current-current correlator: $\int_0^\tau d\tau' \Lambda(\tau')/t \propto \tau^\alpha$ with $\alpha = 2/z - 1$ [2]. This implies a power-law divergence in the optical conductivity, $\sigma(\omega) \propto |\omega|^{-\alpha}$. Reliably extracting α from our data is challenging because we have a relatively short time window over which we can fit the power law: Short-time transients persist to $\tau \sim 10/t$, and our time series only extends to $\tau = 30/t$. Our best fit yields $\alpha \approx 0.3$, with errors that are dominated by systematics and are therefore hard to quantify. This result compares reasonably well with the expected value of $\alpha = 1/3$.

In the opposite limit, $\eta \rightarrow 0$, we find that the conductivity and the relaxation time appear to continuously vanish. This is consistent with an Anderson-localized infinite-temperature state at $\eta = 0$, in which the effective free-particle excitations do not relax. For $\eta < 0.3$, we are unable to reliably extract σ_{DC} or Γ_{DC} from the finite-time current correlations due to large and persistent oscillations in the integrated correlator.

C. Interaction dependence

In Fig. 3(a), we show the integrated time series for a variety of $U/t = 1, 2.5, 5, 10, 15, 20$ at fixed $\eta = 0.5$. In this nonintegrable limit, the relaxation timescales are relatively short and our numerics provide a reasonable estimate for the interaction-dependence of the DC transport properties. Figure 3(b) shows the resistivity, $1/\sigma_{DC}$, as a function of U/t . The resistivity vanishes continuously in the weakly interacting limit, $U/t \rightarrow 0$. Second-order perturbation theory [19,38] suggests that the resistivity should vanish $\propto (U/t)^2$ in this limit, which is consistent with our results. For large U/t , we expect the resistivity to plateau at a finite value, although at $U/t = 20$ it has not yet saturated. Note that this large-interaction limit does not approach a Mott insulator (which would have an infinite resistivity at half filling) because we took the limit of infinite temperature first.

As shown in Fig. 3(c), the transport relaxation rate Γ_{DC} displays similar behavior to the resistivity: it vanishes as $U/t \rightarrow 0$ and plateaus as $U/t \rightarrow \infty$. At weak coupling, one should find a Drude-like relationship between the resistivity and the scattering rate: $1/\sigma_{DC} \propto (m^*/n)_{eff} \Gamma_{DC}$. This suggests

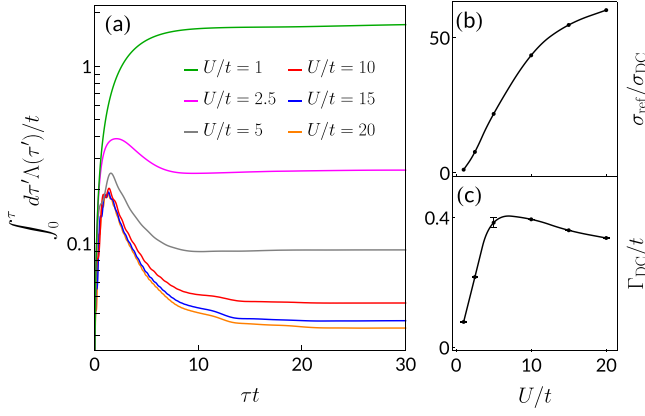


FIG. 3. (a) Integral of $\Lambda(\tau)$ out to finite times for $\eta = 0.5$ and various values of U/t . Note the log scale on the y-axis. (b) DC resistivity (inverse of the conductivity) versus U/t from a fit to panel (a). The resistivity vanishes continuously as we approach the noninteracting limit, $U/t \rightarrow 0$. As $U/t \rightarrow \infty$, the resistivity is expected to plateau at a finite value. (c) Transport decay rate versus U/t from a fit to panel (a). The decay rate vanishes as $U/t \rightarrow 0$ and appears to peak around $U \sim 8t$. As $U/t \rightarrow \infty$, Γ_{DC} approaches a finite η -dependent value.

that $\Gamma_{\text{DC}} \propto U^2/t$, although we are not able to resolve this feature. In the strong-coupling limit, one generically expects the transport scattering rate to saturate at a constant value set by the lattice spacing [38].

IV. ANALYTIC EXPANSION

In the limit $\eta \rightarrow 0$ the heavy particles become frozen, and the interaction term in the Hamiltonian becomes a static disorder potential. The resulting noninteracting model is much simpler than the original. Here we develop an analytic expansion which lets us calculate $\Lambda(\tau)$ for $\eta = 0$ when $U \gg t$.

For a given configuration of the heavy particles, $\{n = n_{i,\downarrow}\}$, the motion of the light particles is controlled by a Hamiltonian

$$\mathcal{H}_0 = -t \sum_i (c_{i,\uparrow}^\dagger c_{i+1,\uparrow} + \text{H.c.}) + \sum_i V(r_i) n_{i,\uparrow}, \quad (10)$$

where $V(r_i) = U \langle n_{i,\downarrow} \rangle$. We can use Wick's theorem to write the current-current correlator of this model in terms of the single-particle Green's functions, $G_{ij}^>(\tau) = \langle c_i(\tau) c_j^\dagger(0) \rangle$ and $G_{ij}^<(\tau) = -\langle c_j^\dagger(0) c_i(\tau) \rangle$:

$$\Lambda_{\{n\}}(x, \tau) = -\frac{t^2}{N_s} \sum_{\substack{i,j,k,l \\ j-i=x}} \eta_{ik} \eta_{jl} G_{i,j}^>(\tau) G_{k,l}^<(-\tau), \quad (11)$$

where

$$\eta_{ik} = \begin{cases} 1 & \text{if } k - i = 1 \\ -1 & \text{if } k - i = -1 \\ 0 & \text{otherwise,} \end{cases} \quad (12)$$

and i, j, k, l are summed over all N_s lattice sites with the constraint that $j - i = x$. We then calculate $\Lambda(x, \tau)$ by performing a disorder average over $\Lambda_{\{n\}}(x, \tau)$.

The potential in Eq. (10) breaks the lattice into a series of disjoint regions over which $V(r_i)$ is constant (either zero or

U). We are interested in the large- U limit: To leading order, a light particle which is placed in one of these regions cannot leave—the energy eigenstates are localized to these regions. Thus the Green's functions G_{ij} vanish unless i and j are in the same region. Equation (11) can then be written as the sum of two terms: $\Lambda^{(0)}$, for which both Green's function describe motion in the same region, and $\Lambda^{(U)}$ where they are in neighboring regions. The former gives dynamics on the timescale $1/t$, while the latter gives dynamics on the scale $1/U$.

As detailed in Appendix C, the resulting spectrum of Λ consists of a sum of δ -function peaks, illustrated in Fig. 1(b). The low-frequency peaks are at energies $\omega = 2t[\cos \pi n/(m+1) - \cos \pi n'/(m+1)]$ where n, n', m are integers with distinct parity (i.e., $n \pm n'$ is odd) with $1 \leq n, n' \leq m$. The parity constraint comes from the symmetry of the current operator, and implies that there is no peak at $\omega = 0$. Here m corresponds to the length of the contributing region. Large- m regions are exponentially suppressed, and the dominant peaks come from $m = 2$ and $m = 3$. This results in the U-shaped distribution of spectral weight, as seen in Fig. 1(b). The high-frequency peaks are at energies $\omega = \pm U + 2t[\cos \pi n/(m+1) - \cos \pi n'/(m+1)]$ where n, n', m , and m' are integers with $1 \leq n \leq m$ and $1 \leq n' \leq m'$. There are no parity constraints and m, m' represent the lengths of neighboring regions. The dominant term comes from $n = n'$, resulting in $\omega = \pm U$. Again, the large m, m' terms are exponentially small.

The analytic peak locations and amplitudes appear to match well the numerical results from our MPS calculations. The broadening of the black curve in Fig. 1(b) comes from the finite time-window of our numerical data.

V. EXPERIMENTAL IMPLEMENTATION

Transport measurements in ultracold atomic systems are in general quite challenging to implement. Recent experiments have managed to measure the DC conductivity via the Einstein relation [29], the optical conductivity via a modulated trap potential [28], and the momentum relaxation rate [27]. Here, we propose an alternative technique to measure the optical conductivity in the *time* domain, and hence $\Lambda(\tau)$ at high temperatures. In this way, our numerical results can be studied directly using the present generation of ultracold atom experiments. Our experimental procedure is schematically illustrated in Fig. 4. After preparing a thermal ensemble, we propose pulsing on a lattice tilt, $H_{\text{tilt}}(\tau) = F(\tau) \sum_l l n_l$, for a short time, W . In quantum gas microscopes, this linear potential can be realized from the AC Stark shift at the edge of a wide Gaussian beam [49]. Generically, this pulsed tilt will generate a current response given by $\langle J \rangle(\beta, \omega) = \sigma(\beta, \omega) \tilde{F}(\omega)$, where $\tilde{F}(\omega)$ is the Fourier transform of $F(\tau)$ and $\sigma(\beta, \omega)$ is the optical conductivity at inverse temperature β . In the limit that the pulse duration $W \rightarrow 0$, we can approximate $F(\tau) \approx F_0 W \delta(\tau)$, and hence the real-time current response is given by $\langle J \rangle(\beta, \tau) = F_0 W \sigma(\beta, \tau)$. In the high-temperature $\beta \rightarrow 0$ limit, then, we use Eq. (6) to find

$$\langle J \rangle(\beta, \tau) \approx \frac{\beta F_0 W}{2} \Lambda(\tau). \quad (13)$$

In quantum gas microscopes, the expectation value of the current operator can be measured by releasing the atoms

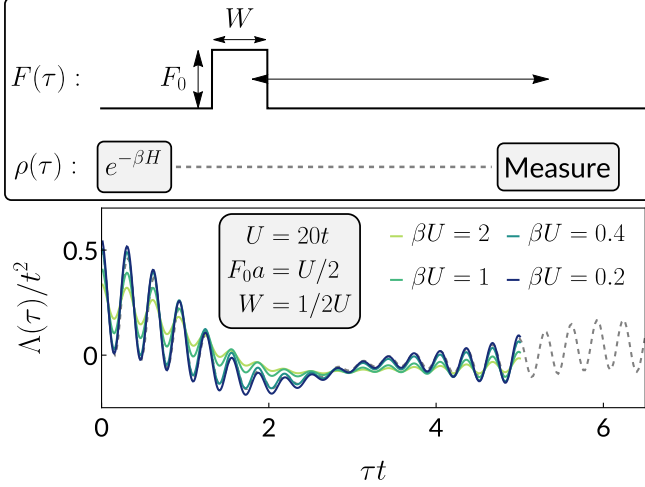


FIG. 4. Experimental sequence for measuring current-current correlations in an ultracold atomic gas. (top) After preparing a thermal ensemble, one pulses on a lattice tilt for time T . One then allows the system to evolve for time τ and measures the momentum distribution using time of flight (see main text). (bottom) Benchmarking this procedure using the TDVP algorithm on a 30-site lattice using Eq. (13). Solid curves show TDVP calculations for various parameters. Simulations approach the infinite-system, infinite-temperature results (gray dashed line) when the parameters F_0a/U , WU , and βU are made small. Dashed curve is continued to longer times for visual clarity.

from their trapping potential, allowing them to expand and thus mapping their *in situ* momenta to position space [25,26]. Once the momentum distribution function $\langle n_{k,\mu} \rangle$ is known, the expectation value of the current is simply $\langle J \rangle = \sum_{k,\mu} t_\mu \sin(k) \langle n_{k,\mu} \rangle$.

In the bottom panel of Fig. 4, we show the results of this procedure simulated with the finite-size time-dependent variational principle (TDVP) algorithm [50] on a 30-site lattice for $U/t = 20$ and various values of β . This modeling captures experimental finite-size effects, as well as the influence of detailed pulse shapes. As noted above, our results emerge in the $\beta \rightarrow 0$ limit; finite- β corrections yield additional information about the full optical conductivity $\sigma(\beta, \tau)$. We find that the results agree well with our infinite calculations so long as βU , WU , and F_0a/U are all $\lesssim 1$ (assuming $U \gg t$).

This proposed experimental procedure yields the conductivity at any temperature. Comparison with our theoretical results, however, is predicated on the simultaneous validity of the single-band approximation and the high-temperature limit. This requires $W \ll T \ll \Delta$, where Δ is the band gap and W is the bandwidth. Both W and Δ can be estimated by solving the single-particle Schrödinger equation in a sinusoidal potential $V(x) = V_0 \cos^2(k_R x)$. The ytterbium experiment [20] was performed with $V_0 = 7E_R$, where $E_R = \hbar^2 k_R^2 / 2m$. This leads to $W/\Delta \approx 0.05$, indicating that there is a temperature regime where our single-band high-temperature expansion is relevant.

VI. CONCLUSIONS AND OUTLOOK

In this paper, we have provided a comprehensive study of the moderate-time transport properties of the

one-dimensional mass-imbalanced Fermi-Hubbard model in the high-temperature limit. This model serves as a valuable setting for exploring the interplay of integrability and localization.

By studying the strongly interacting and heavily imbalanced limit, we have mapped out the resonances associated with bound excitations of heavy and light particles. Our analytic model provides a precise account of these nontrivial finite-frequency features, which we have benchmarked against state of the art time-dependent MPS simulations. In the strongly interacting and weakly imbalanced limit, we found that the DC conductivity diverges continuously as $\eta \rightarrow 1$. At the symmetric point, superdiffusive correlations lead to a power-law divergence in the integrated correlator as a function of time. This corresponds to a power-law divergence in the optical conductivity, $\sigma(\omega) \propto |\omega|^{-\alpha}$. We estimate the exponent of this divergence to be $\alpha \approx 0.3$, close to the KPZ prediction of $\alpha = 1/3$.

Many interesting questions regarding this model remain outstanding. While there is good reason to believe that the mass-imbalanced model is ergodic for $\eta > 0$ [14–17], directly studying the onset of diffusive transport is challenging. Questions persist about the long-lived nature of bound states and whether intermediate-scale subdiffusive regimes exist prior to thermalization [16,20]. Similar questions exist near the symmetric limit: How does the characteristic time for the onset of diffusion, τ_D , behave as $\eta \rightarrow 1$ in the strongly correlated limit? The timescales on which these questions can be answered are not accessible with the current generation of numerical tools, and it will require further theoretical and experimental insights to probe these regimes [51–53]. Our experimental proposal provides one possible approach.

ACKNOWLEDGMENT

This work was supported by the NSF Grant No. PHY-2110250.

APPENDIX A: DETAILS OF MATRIX PRODUCT STATE CALCULATION

1. Matrix product state purification

To model the properties of the infinite-temperature current-current correlation function, we first purify the density matrix so that it can be represented as an infinite matrix product state (iMPS). This is a standard technique, so we refer the interested reader to Ref. [40] for a thorough review. In this section, we give a brief introduction to purification and then describe the procedure that we use for incorporating number conservation.

The infinite-temperature density matrix, ρ_0 , is simply a diagonal operator acting on the physical Hilbert space of the Hamiltonian:

$$\rho_0 = \prod_i \left[\frac{1}{\mathcal{N}_i} \sum_{s_i, s'_i} \delta_{s_i, s'_i} y(s_i) |s_i\rangle \langle s'_i| \right], \quad (\text{A1})$$

where i indexes lattice sites and $s_i, s'_i \in \{\uparrow, \downarrow, \emptyset, \uparrow\downarrow\}$ span the local Hilbert space on site i . Importantly, this form of ρ_0

shows that distinct sites i and j are completely uncorrelated. The quantity $y(s_i)$ is the fugacity and \mathcal{N}_i is the normalization enforcing $\text{Tr}\rho_0 = 1$. At infinite temperature, zero magnetization and a fixed particle density \bar{n} , we have $y(\uparrow) = y(\downarrow) = \bar{n}/(2 - \bar{n})$, $y(\emptyset) = 1$, and $y(\uparrow\downarrow) = y(\uparrow)y(\downarrow)$, which means $\mathcal{N}_i = [1 + y(\uparrow\downarrow)]^2$.

We now introduce an auxiliary set of states, labeled by quantum number $\{t\}$, which expand our Hilbert space and allow us to represent the density matrix as $\rho_0 = \text{Tr}_{\{t\}}|\psi_0\rangle\langle\psi_0|$. The simplest such representation is

$$|\psi_0^{\text{triv}}\rangle = \prod_i \left[\frac{1}{\sqrt{\mathcal{N}_i}} \sum_{s_i, t_i} \delta_{s_i, t_i} \sqrt{y(s_i)} |s_i\rangle \otimes |t_i\rangle \right]. \quad (\text{A2})$$

Here i indexes the physical sites, as before, but now it is associated with *two* sites: the same physical one, whose state is denoted by s_i , and the associated auxiliary one, whose state is denoted by t_i . We refer to this as a trivial purification because it fixes the state of the physical site s_i to be identical to that of the auxiliary site t_i .

As explained in Sec. A2 it is convenient to construct alternative purifications via unitary transformations on the auxiliary subspace. These will make it easier to encode conservation laws. Explicitly,

$$\begin{aligned} |\psi_0(U)\rangle &= U^\dagger |\psi_0^{\text{triv}}\rangle \\ &= \prod_i \left[\frac{1}{\sqrt{\mathcal{N}_i}} \sum_{s_i, t_i} \delta_{s_i, t_i} U *_{t_i, t_i} \sqrt{y(s_i)} |s_i\rangle \otimes |\tilde{t}_i\rangle \right] \\ &= \prod_i \left[\frac{1}{\sqrt{\mathcal{N}_i}} \sum_{s_i, t_i} U *_{t_i, s_i} \sqrt{y(s_i)} |s_i\rangle \otimes |t_i\rangle \right]. \end{aligned} \quad (\text{A3})$$

For arbitrary unitary transformations, the infinite-temperature density matrix can be written as a partial trace over the auxiliary degrees of freedom:

$$\begin{aligned} \rho_0 &= \text{Tr}_{\{t, t'\}} |\psi_0(U)\rangle\langle\psi_0(U)| \\ &= \prod_i \left[\frac{1}{\mathcal{N}_i} \sum_{s_i, s'_i, t_i, t'_i} \sqrt{y(s_i)y(s'_i)} U *_{t_i, s_i} |s_i\rangle\langle t_i| t'_i\rangle\langle s'_i| U_{t'_i, s'_i} \right] \\ &= \prod_i \left[\frac{1}{\mathcal{N}_i} \sum_{s_i, s'_i} \delta_{s_i, s'_i} y(s_i) |s_i\rangle\langle s'_i| \right]. \end{aligned} \quad (\text{A4})$$

2. Symmetries

One often uses conservation laws to write MPS tensors in a block-sparse form, speeding up the calculations [40,43]. In our case, the Fermi-Hubbard model conserves both total magnetization and total particle number: $U_{\text{part}}(1) \otimes U_{\text{spin}}(1)$. For the wave function on the doubled Hilbert space, then, we should double the symmetry: $U_{\text{part}}^{\text{phys}}(1) \otimes U_{\text{part}}^{\text{aux}}(1) \otimes U_{\text{spin}}^{\text{phys}}(1) \otimes U_{\text{spin}}^{\text{aux}}(1)$. Unfortunately, total magnetization and particle number are explicitly not conserved for $|\psi_0(U)\rangle$ because it represents a purified grand-canonical density matrix. Working in the canonical ensemble is intractable, as that leads to a MPS whose bond dimension scales with the system size

[43]. Nonetheless, we can take advantage of some of the symmetry: In the trivial purification, for each spin state the number of auxiliary particles equals the number of physical particles. A convenient way to keep track of this symmetry is to introduce a particle-hole transformation on the auxiliary particles, $U = \prod_i U_i$, where

$$U_i = \begin{pmatrix} 0 & 1 & 0 & 0 \\ -1 & 0 & 0 & 0 \\ 0 & 0 & 0 & -1 \\ 0 & 0 & 1 & 0 \end{pmatrix} \quad (\text{A5})$$

is written in the basis introduced above: $(\uparrow, \downarrow, \emptyset, \uparrow\downarrow)$. This results in a purified state of the form

$$\begin{aligned} |\psi_0(U)\rangle &= \prod_i \left[\frac{1}{\sqrt{\mathcal{N}_i}} \left(-\sqrt{y(\uparrow\downarrow)} |\uparrow\downarrow\rangle_{\text{phys}} |\emptyset\rangle_{\text{aux}} \right. \right. \\ &\quad \left. \left. + \sqrt{y(\emptyset)} |\emptyset\rangle_{\text{phys}} |\uparrow\downarrow\rangle_{\text{aux}} - \sqrt{y(\uparrow)} |\uparrow\rangle_{\text{phys}} |\downarrow\rangle_{\text{aux}} \right. \right. \\ &\quad \left. \left. + \sqrt{y(\downarrow)} |\downarrow\rangle_{\text{phys}} |\uparrow\rangle_{\text{aux}} \right) \right]. \end{aligned} \quad (\text{A6})$$

As one sees explicitly, in this representation the total number of particles (physical plus auxiliary), and their net spin, is fixed. Hence we can introduce the associated quantum numbers, and all tensors in our MPS calculation will have block-sparse forms. The minus signs are chosen to simplify the construction in Sec. A3.

3. Auxiliary operators

The fact that ρ_0 is diagonal means that its purification has a special property: any operator \hat{O}_{phys} that acts on the physical degrees of freedom of $|\psi_0(U)\rangle$ has a partner, \hat{O}'_{aux} , acting on just the auxiliary degrees of freedom, such that [42]

$$\hat{O}_{\text{phys}} \otimes \mathbb{I}_{\text{aux}} |\psi_0(U)\rangle = \mathbb{I}_{\text{phys}} \otimes \hat{O}'_{\text{aux}} |\psi_0(U)\rangle. \quad (\text{A7})$$

The relationship between \hat{O} and \hat{O}' depends on the choice of purification, $|\psi_0(U)\rangle$: $\hat{O}' = U^\dagger \hat{O} U$. As argued in the main text, determination of the auxiliary Hamiltonian can significantly decrease the computational complexity of time evolution by allowing one to shift the purification insertion point [41]. In our case, the choice of unitary in Eq. (A5) implies that the auxiliary Hamiltonian (at half filling) is simply the particle-hole transform of the physical one:

$$\begin{aligned} U^\dagger \hat{c}_\mu U &= -\hat{c}_\mu^\dagger, \\ U^\dagger \hat{n}_\mu U &= 1 - \hat{n}_\mu. \end{aligned} \quad (\text{A8})$$

4. Time evolution with infinite boundary conditions

The numerical technique we employ is based on the dynamically expanding window technique developed in Refs. [44–46], and we refer interested readers to these references. In this section we give a high level discussion of a number of details, explaining the major bottlenecks. To calculate our response function, we apply the local current operator $j(0) = -it(c_1^\dagger c_0 - c_0^\dagger c_1)$ to the infinite matrix product state described by Eq. (A7). This is a local perturbation that just influences sites $l = 0, 1$. As discussed in the main text, we then time-evolve this wave function using the Liouvillian,

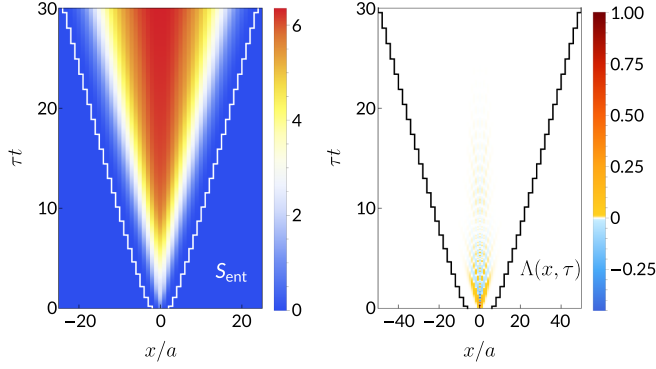


FIG. 5. Heat map of the entanglement entropy, $S_{\text{ent}}(x, \tau)$ (left), and current-current correlator, $\Lambda(x, \tau)$ (right), as a functions of position and time. On both plots, the effective length of the MPS is shown as a solid jagged line: the white line in (left) is equal to the number of physical sites at a given time, while the black line in (right) is double the number of physical sites (as we take all possible overlaps between two length- L MPS, see Appendix A 4).

$\mathcal{L} = H_{\text{phys}} - H'_{\text{aux}}$, to produce

$$|\psi(0, \tau)\rangle = e^{i\mathcal{L}\tau} j_0 |\psi_0\rangle. \quad (\text{A9})$$

At any finite time τ , the matrix product state representation of $|\psi(0, \tau)\rangle$ will differ from $|\psi_0\rangle$, only over a region of size $l_0(\tau)$, centered at the origin. The perturbed region grows linearly with time, describing a light cone. In our calculation we start with an infinite matrix product state ansatz where all but $l_0(\tau = 0) = 6$ of the matrices have the form Eq. (A7). As described in the main text, we use a third-order split step W^H time evolution algorithm, where we sweep back and forth through this active region, updating the l_0 matrices. We increase l_0 when the entanglement entropy between the bulk and boundary sites surpasses $\epsilon_{\text{thresh}} = 10^{-5}$ [44–46]. Figure 5(a) shows the evolution of the entanglement entropy of the purified wave function during this process, for $U/t = 20$ and $\eta = 0.5$. The white line shows the spatial extent of the active region, outside of which the MPS tensors correspond to those in Eq. (A7). The light-cone spreading of the entanglement is clear. Note that this entanglement entropy is a property of the purified wave function, rather than of the physical density matrix. Nonetheless, it illustrates the key numerical bottleneck in our calculation: The peak entanglement entropy grows linearly in time, and hence the required bond dimension grows exponentially [54]. To calculate the current-current correlator, we relabel our sites to produce the translated state $\hat{T}_x |\psi(0, \tau)\rangle = |\psi(x, \tau)\rangle$. The current-current correlator is then found by calculating the overlap between the shifted and original states,

$$\Lambda(x, \tau) = \langle \psi * (0, \tau/2) | \psi(x, \tau/2) \rangle. \quad (\text{A10})$$

In practice, the translation is implemented by temporarily appending unevolved sites to the end of the chains. Given the product state on the wings of purified wave function, for $x > 2l_0 - 1$ the correlator trivially factors into

$$\Lambda(x > 2l_0 - 1, \tau) = \langle \psi * (0, \tau/2) | \psi_0 \rangle \langle \psi_0 | \psi(x, \tau/2) \rangle, \quad (\text{A11})$$

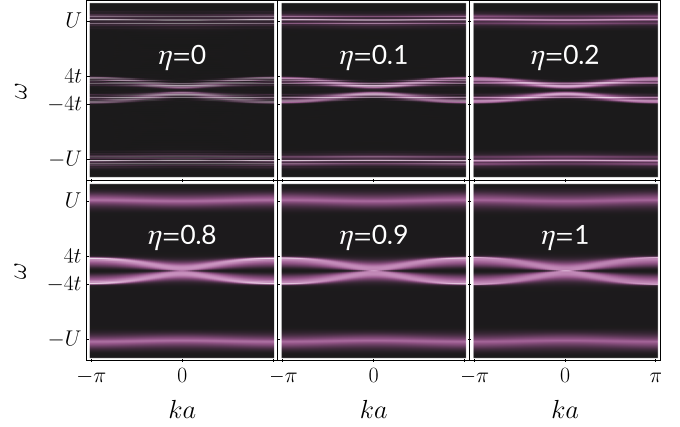


FIG. 6. Infinite-temperature current-current correlation functions in the Fourier domain, $\Lambda(k, \omega)$, at $U/t = 20$ and a range of imbalances. At $\eta = 0$ we resolve a series of δ function contributions (see Sec. IV) that vary continuously with k . As argued in Appendix C, spectral weight is confined around $\omega = 0$ and $\omega = \pm U$. As η increases, these δ functions broaden. As $\eta \rightarrow 1$, sharp low-frequency features appear near $k = 0$ and $k = \pm\pi$, while the $\omega \sim U$ excitations become weakly dispersive.

which vanishes due to the absence of equilibrium currents. Figure 5(b) shows the current-current correlator inside this expanding window. One sees rapid oscillations, with timescale $\sim 1/U$, inside an envelope which decays on a timescale of order several $1/t$. Visually, the current correlations do not appear to spread significantly, but instead remain confined to a central region of ≈ 20 sites. By Fourier transforming the data in Fig. 5, we can calculate $\Lambda(k, \omega)$, which gives the frequency and momentum dependence of the current correlations. Figure 6 shows $\Lambda(k, \omega)$ for $U/t = 20$ and a variety of mass imbalances. One clearly sees structures on two frequency scales: low-frequency contributions bounded by $\pm 4t$, and high-frequency contributions near $\omega \sim \pm U$. This same structure is apparent in the time domain in Fig. 5 and is described in more detail in Appendix C for $\eta = 0$. For small η one sees a fine structure of bands, whose frequencies correspond to the δ -functions in the optical conductivity. For $\eta = 0$ the spectral weight associated with $\omega \sim U$ is independent of k . This indicates that the associated excitations are localized. These correspond to processes where the current operator has created or broken up a doublon. At larger η the momentum-resolved spectra are smooth. The bands with $\omega \sim \pm U$ are weakly dispersing because the doublons can hop with an effective matrix element $t_{\text{eff}} \sim \eta^2/U$. As $\eta \rightarrow 1$, we resolve a cusp in the optical conductivity near $\omega, k = 0$ arising due to superdiffusive fluctuations at the highly symmetric, integrable point [9]. According to Eq. (6) the DC conductivity can be found from $\Lambda(k, \omega)$ by taking the limit $\omega \rightarrow 0$ at fixed $k = 0$, $\sigma_{\text{DC}} = \sigma_{\text{ref}} \lim_{\omega \rightarrow 0} \Lambda(k = 0, \omega)$, where $\sigma_{\text{ref}} = \alpha\beta t$. Conversely, at fixed $k \neq 0$ one expects $\Lambda(k, \omega = 0) = 0$, as a static longitudinal electric field with zero mean cannot generate equilibrium currents. Thus the limits $k \rightarrow 0$ and $\omega \rightarrow 0$ do not commute. This singular structure is smoothed out by our finite time effects. Nonetheless, in the larger η data in Fig. 6, one sees different behavior when approaching the

origin from different directions. The apparent spectral gap at small but nonzero η is a finite-time artifact.

APPENDIX B: POWER-LAW CORRELATIONS

Here we provide a derivation of the relationship between the dynamical scaling exponent, z and the power-law exponent of the integrated current-current correlator, α , presented in Sec. III. Equivalent expressions can be found in Ref. [2]. Given that particle and spin densities are conserved in our system, a local density disturbance will spread out with width $W^2(\tau) = \int dx x^2 \delta n_\uparrow(x, \tau)$ scaling as $W^2(\tau \rightarrow \infty) \propto \tau^{2/z}$, where z is the dynamical exponent [2,55]. For ballistic transport $z = 1$, while for diffusive transport $z = 2$. This behavior is also found in the density-density correlation function,

$$C_{\uparrow\uparrow}(x, \tau) = \frac{1}{N_s} \sum_i \langle n_\uparrow(i+x, \tau) n_\uparrow(i, 0) \rangle, \quad (\text{B1})$$

which by the fluctuation-dissipation theorem can be related to the density response of the system to a local potential. As such, we can define

$$\Sigma_{\uparrow\uparrow}^2(\tau) = \sum_x x^2 C_{\uparrow\uparrow}(x, \tau) - \left(\sum_x x C_{\uparrow\uparrow}(x, \tau) \right)^2, \quad (\text{B2})$$

which encodes the width of a density disturbance following a local perturbation. Hence, it too obeys $\Sigma_{\uparrow\uparrow}^2(\tau) \propto \tau^{2/z}$ in the long-time (hydrodynamic) limit [2,55]. For notational simplicity, we leave off the subscript \uparrow , and calculate the rate of change of $\partial_\tau^2 \Sigma^2(\tau) = \sum_x x^2 \partial_\tau^2 \langle n(x, \tau) n(x, 0) \rangle$. Using time-translational invariance and reflection symmetry, we can rewrite this as

$$\partial_\tau^2 \Sigma^2(\tau) = - \sum_x x^2 \langle \partial_{\tau_1} n(x, \tau_1) \partial_{\tau_2} n(0, \tau_2) \rangle, \quad (\text{B3})$$

evaluated at $\tau_1 = \tau$ and $\tau_2 = 0$. We then relate the time derivatives of the densities to the current, $\partial_\tau n(x, \tau) = j(x+1, \tau) - j(x, \tau)$, and rearrange the sum to connect Σ^2 to the current-current correlator:

$$\partial_\tau^2 \Sigma^2(\tau) = 2 \sum_x \langle j(x, \tau) j(0, 0) \rangle = 2\Lambda(\tau). \quad (\text{B4})$$

Given that $\Sigma^2(\tau) \propto \tau^{2/z}$, Eq. (B4) yields $\Lambda(\tau) \propto \tau^{2/z-2}$. Hence, the integrated current-current correlator should scale as τ^α with $\alpha = 2/z - 1$. This same exponent describes the associated low-frequency behavior of the optical conductivity: $\sigma(\omega) \propto |\omega|^{-\alpha}$ [2]. For generic mass imbalance we expect $z = 2$ and hence $\alpha = 0$. At $\eta = 1$, KPZ scaling predicts $z = 3/2$ and hence $\alpha = 1/3$.

APPENDIX C: DETAILS OF ANALYTIC EXPANSION

In the Falicov-Kimball limit $\eta \rightarrow 0$, the mass-imbalanced Hubbard Hamiltonian reduces to

$$H_0 = -t \sum_i (c_{i,\uparrow}^\dagger c_{i+1,\uparrow} + \text{H.c.}) + U \sum_i n_{i,\uparrow} n_{i,\downarrow}. \quad (\text{C1})$$

As noted in the main text, the Hamiltonian H_0 commutes with the \downarrow particle density on every lattice site, $[H_0, n_{i,\downarrow}] = 0$, so the \downarrow -spin densities on each site are conserved. For a given

configuration of \downarrow spins, $\{n\} = \{n_{i,\downarrow}\}$, the effective Hamiltonian for the \uparrow spins is

$$\mathcal{H}_0 = -t \sum_i (c_{i,\uparrow}^\dagger c_{i+1,\uparrow} + \text{H.c.}) + \sum_i V(r_i) n_{i,\uparrow}, \quad (\text{C2})$$

where $V(r_i) = U n_{i,\downarrow}$. The fact that Eq. (C2) is quadratic in the fermion operators means that its properties can be exactly calculated. Using Wick's theorem, we write the current-current correlation function as

$$\Lambda_{\{n\}}(x, \tau) = -\frac{t^2}{N_s} \sum_{\substack{i,j,k,l \\ j-i=x}} \eta_{ik} \eta_{jl} G_{i,j}^>(\tau) G_{k,l}^<(-\tau), \quad (\text{C3})$$

where

$$\eta_{ik} = \begin{cases} 1 & \text{if } k - i = 1 \\ -1 & \text{if } k - i = -1 \\ 0 & \text{otherwise,} \end{cases} \quad (\text{C4})$$

and i, j, k, l are summed over all N_s lattice sites with the constraint that $j - i = x$. Here $G_{ij}^>(\tau) = \langle c_i(\tau) c_j^\dagger(0) \rangle$ and $G_{ij}^<(\tau) = -\langle c_j^\dagger(0) c_i(\tau) \rangle$ are the single-particle Green's functions, whose dependence on $\{n\}$ has been suppressed. Throughout we consider the strong-coupling limit where $U \gg t$.

1. Decomposition into regions of fixed n_\downarrow

The configuration of \downarrow spins acts as a binary disorder potential. Even infinitesimal disorder should Anderson-localize all the single-particle wave functions. In the regime of interest, $U \gg t$, the localization length is very short, and the single-particle wave functions are confined to regions of constant background potential, i.e., contiguous sequences of sites for which n_\downarrow is constant. Hence, the Green's functions should vanish unless i and j are in the same region, Ω , and k, l are in the same region, Ω' . Due to the constraints from the η , we then have two possibilities: either $\Omega = \Omega'$, or Ω, Ω' are neighboring regions. This leads to the decomposition

$$\begin{aligned} \Lambda_{\{n\}}(x, \tau) = & -\frac{t^2}{N_s} \sum_{\Omega} \sum_{\substack{i,j,k,l \in \Omega \\ j-i=x}} \eta_{ik} \eta_{jl} G_{i,j}^>(\tau) G_{k,l}^<(-\tau) \\ & -\frac{t^2}{N_s} \sum_{(\Omega, \Omega')} \sum_{\substack{i,j \in \Omega \\ k,l \in \Omega' \\ j-i=x}} \eta_{ik} \eta_{jl} \\ & \times [G_{i,j}^>(\tau) G_{k,l}^<(-\tau) + G_{k,l}^>(\tau) G_{i,j}^<(-\tau)], \end{aligned} \quad (\text{C5})$$

which can be expressed as

$$\begin{aligned} \Lambda_{\{n\}}(x, \tau) = & \frac{1}{N_s} \sum_{\Omega} m \Lambda_m^{(0)}(x, \tau) \\ & + \frac{1}{N_s} \sum_{(\Omega, \Omega')} \left(\frac{m+m'}{2} \right) \Lambda_{mm'}^{(U)}(x, \tau), \end{aligned} \quad (\text{C6})$$

where m is the length of segment Ω and m' is the length of segment Ω' . The summands only depend on the lengths of the segments,

$$\Lambda_m^{(0)}(x, \tau) = -\frac{t^2}{m} \sum_{\substack{i,j,k,l=1 \\ j-i=x}}^m \eta_{ik} \eta_{jl} G_{ij}^>(\tau) G_{kl}^<(-\tau), \quad (\text{C7})$$

$$\Lambda_{mm'}^{(U)}(x, \tau) = -\frac{2t^2}{m+m'} \delta_{x,0} [G_{11}^>(\tau) G_{00}^<(-\tau) + G_{00}^>(\tau) G_{11}^<(-\tau)]. \quad (\text{C8})$$

In Eq. (C7) we have used translational invariance to take the region $\Omega = [1, 2, \dots, m]$ to extend between sites 1 through m . In Eq. (C8) we take Ω to be to the left of Ω' , with $\Omega = [-m+1, -m+2, \dots, 0]$ and $\Omega' = [1, 2, \dots, m']$. The factors of m and m' in Eq. (C6) are chosen for notational convenience: $\sum_{\Omega} m = N_s$ and $\sum_{(\Omega, \Omega')} (m+m') = 2N_s$, as long as $\{n\}$ contains at least two regions. We now wish to rewrite the sum of Ω in Eq. (C6) as a sum over m . We note that at infinite temperature, each site is independent and the probability of any given site containing a heavy (\downarrow) particle is equal to \bar{n}_{\downarrow} , the average density of heavy particles. Consequently, the probability that a given site is in region containing m adjacent \downarrow spins is $P_m = m(1 - \bar{n}_{\downarrow})^2 \bar{n}_{\downarrow}^m$. The factor of m accounts for the m different possible ways the region could contain that site. The \bar{n}_{\downarrow}^m is due to the fact that we need m sites which each contain a \downarrow spin. The $(1 - \bar{n}_{\downarrow})^2$ comes from the fact that the region must be bookended by empty sites. Similarly the probability that a site is in a region of m empty sites is $\bar{P}_m = m \bar{n}_{\downarrow}^2 (1 - \bar{n}_{\downarrow})^m$. One can readily verify that $\sum_m (P_m + \bar{P}_m) = 1$. Finally we note that the total number of regions of length m should be $\mathcal{N}_m = N_s (P_m + \bar{P}_m) / m$ and for any function f_m ,

$$\sum_{\Omega} f_m = \sum_m \mathcal{N}_m f_m = N_s \sum_m (P_m + \bar{P}_m) \frac{f_m}{m}. \quad (\text{C9})$$

We can apply an analogous argument to thinking about consecutive regions with Ω of length m to the left of Ω' of length m' . If Ω is comprised of \downarrow spins and Ω' of empty sites, the probability that an individual site is within this configuration is $P_{mm'} = (m+m') \bar{n}_{\downarrow}^{m+1} (1 - \bar{n}_{\downarrow})^{m'+1}$. The probability of a site being in the complementary configuration (where Ω is comprised of empty sites and Ω' of \downarrow spins) is $\bar{P}_{mm'} = (m+m') \bar{n}_{\downarrow}^{m'+1} (1 - \bar{n}_{\downarrow})^{m+1}$. Hence the total number of such configurations is $\mathcal{N}_{mm'} = N_s (P_{mm'} + \bar{P}_{mm'}) / (m+m')$, and

$$\sum_{(\Omega, \Omega')} f_{mm'} = \sum_{mm'} \mathcal{N}_{mm'} f_{mm'} = N_s \sum_{mm'} (P_{mm'} + \bar{P}_{mm'}) \frac{f_{mm'}}{m+m'}. \quad (\text{C10})$$

We can then rewrite Eq. (C6) as

$$\Lambda(x, \tau) = \underbrace{\sum_m (P_m + \bar{P}_m) \Lambda_m^{(0)}(x, \tau)}_{\Lambda^{(0)}(x, \tau)} + \frac{1}{2} \underbrace{\sum_{m,m'} (P_{mm'} + \bar{P}_{mm'}) \Lambda_{mm'}^{(U)}(x, \tau)}_{\Lambda^{(U)}(x, \tau)}. \quad (\text{C11})$$

In the subsequent sections, we evaluate the terms $\Lambda_m^{(0)}$ and $\Lambda_{mm'}^{(U)}$ analytically in the limit $U \gg t$. This calculation is more natural in momentum space, so we introduce the Fourier transform $\Lambda(q, \tau) = \sum_x e^{iqx} \Lambda(x, \tau)$.

2. Spectral representation

At infinite temperature, $G_{ij}^>(\tau) = (1 - \bar{n}_{\uparrow}) A_{ij}(\tau)$ and $G_{ij}^<(\tau) = -\bar{n}_{\uparrow} A_{ij}(\tau)$, with spectral function $A_{ij}(\tau) = \sum_{\nu} \psi_i^{\nu} (\psi_j^{\nu})^* e^{-i\epsilon_{\nu} \tau}$. Here we use ν to label the single-particle eigenstates. In our case the \uparrow particle density is $\bar{n}_{\uparrow} = 1/2$. Let us now consider a region of m sites with $V = 0$, surrounded by sites with $V = U$. We treat these as effective hard-wall boundary conditions, labeling the sites in the constant-potential region as $i = 1, 2, \dots, m$. The single-particle eigenstates are given by $\psi_i^n = A \sin ki$ where $k = \pi n / (m+1)$; the integer n can take values $1, 2, \dots, m$. Note that we mix our notation and use k and n interchangeably, for example, defining the energy $v_n = -2t \cos k$, which should be interpreted as $v_n = -2t \cos \pi n / (m+1)$. The normalization factor is $|A|^2 = 2 / (m+1)$. Eigenstates in an analogous high-potential region are identical, with energies just shifted by U . One consequence is that $\Lambda^{(0)}$ captures the dominant low-frequency contributions to Λ , while $\Lambda^{(U)}$ contains frequency components which are of order U .

3. Low-frequency contributions: $\Lambda^{(0)}$

We first compute the low-frequency contributions $\Lambda_m^{(0)}(q, \tau) = \sum_x e^{iqx} \Lambda_m^{(0)}(x, \tau)$ from regions of size m to the current-current correlator [see Eq. (C11)]. To begin, we return to the definition of $\Lambda_m^{(0)}$ in Eq. (C7). Evaluating the factors of η_{ik} ,

$$\Lambda_m^{(0)}(q, \tau) = \frac{t^2 \bar{n}_{\uparrow} (1 - \bar{n}_{\uparrow})}{m} \times \sum_{l,j=1}^{m-1} e^{iq(l-j)} (A_{l,j}^+ A_{j+1,l+1}^- - A_{l+1,j}^+ A_{j+1,l}^- + A_{l+1,j+1}^+ A_{j,l}^- - A_{l,j+1}^+ A_{j,l+1}^-), \quad (\text{C12})$$

where $A_{l,j}^+ = A_{l,j}(\tau)$ and $A_{l,j}^- = A_{l,j}(-\tau)$. If we expand $A_{l,j}$ in terms of single-particle wave functions and collect terms with the same site index, this can be rewritten as

$$\Lambda_m^{(0)}(q, \tau) = \frac{t^2 \bar{n}_{\uparrow} (1 - \bar{n}_{\uparrow})}{m} \sum_{n, \bar{n}=1}^m e^{i(v_n - v_{\bar{n}}) \tau} \times [C_{\bar{n}n}(q) C_{\bar{n}n}(-q) + C_{n\bar{n}}(q) C_{n\bar{n}}(-q) - C_{\bar{n}\bar{n}}(q) C_{\bar{n}\bar{n}}(-q) - C_{nn}(q) C_{nn}(-q)]. \quad (\text{C13})$$

where $C_{\bar{n}n}(q) = \sum_{l=0}^m e^{ilq} \psi_l^{\bar{n}} \psi_{l+1}^n$. Evaluating $\Lambda_m^{(0)}(q, \tau)$ now amounts to evaluating $C_{\bar{n}n}(q)$. Inserting the explicit form of the single-particle wave functions and summing over l yields

$$C_{\bar{n}n}(q) = -\frac{A^2}{4} [\Upsilon(k + \bar{k} + q) e^{i\bar{k}q} + \Upsilon(-k - \bar{k} + q) e^{-i\bar{k}q} - \Upsilon(k - \bar{k} + q) e^{-i\bar{k}q} - \Upsilon(-k + \bar{k} + q) e^{i\bar{k}q}]. \quad (\text{C14})$$

with

$$\Upsilon(p) = \frac{1 - e^{i(m+1)p}}{1 - e^{ip}}. \quad (\text{C15})$$

Following the notation introduced in Sec. C 2, $k = \pi n/(m+1)$ and $\bar{k} = \pi \bar{n}/(m+1)$. While the expression in Eq. (C14) can be used to numerically calculate the response function for arbitrary q , it is cumbersome to work with analytically. We can, however, simplify it when $q = 0$ or $q = \pi$. The former results are quoted in the main text. We first take $q = 0$. Note that because of the form of the momentum the phase factor in the numerator obeys $e^{i(m+1)p} = \pm 1$. If $p = 0$, corresponding to $n = \bar{n}$, then both the numerator and denominator vanish, and by using L'Hôpital's rule, we see that $\Upsilon(0) = m+1$. Otherwise $\Upsilon(p)$ is nonzero only for odd p , corresponding to n and \bar{n} having opposite parity. The $p = 0$ terms cancel with one-another when substituted into Eq. (C13), so we only need to consider the terms where n and \bar{n} have opposite parity, i.e., $e^{\pm i(k \pm \bar{k})(m+1)} = -1$. After a bit of algebra, one finds

$$C_{\bar{n}n}(0) = \frac{1}{m+1} \left(\frac{\sin(k - \bar{k})/2}{\sin(k + \bar{k})/2} - \frac{\sin(k + \bar{k})/2}{\sin(k - \bar{k})/2} \right), \quad (\text{C16})$$

$\times (n + \bar{n}) \text{ odd.}$

Clearly $C_{\bar{n}n}(0)$ is odd when one switches n and \bar{n} , so the contribution to the uniform current-current correlator can be written as

$$\Lambda_m^{(0)}(0, \tau) = \frac{4t^2 \bar{n}_\uparrow (1 - \bar{n}_\uparrow)}{m} \sum_{\bar{n}\bar{n}}' e^{i(v_n - v_{\bar{n}})\tau} [C_{\bar{n}n}(0)]^2, \quad (\text{C17})$$

where the prime indicates that we just include terms with opposite parity. The full low-energy contribution can now be found by inserting Eq. (C17) into Eq. (C11). To calculate the correlator numerically, as we do in the main text, we simply truncate the m sum to be finite. In Fig. 1, we truncate $\Lambda^{(0)}$ at $m = 30$. A similar argument holds for $\Lambda_m^{(0)}(\pi, \tau)$, and we find

$$\Lambda_m^{(0)}(\pi, \tau) = \frac{t^2 \bar{n}_\uparrow (1 - \bar{n}_\uparrow)}{m} \sum_{n=1}^m e^{-2i\tau v_n} v_n^2. \quad (\text{C18})$$

Note that this only involves frequencies which are an even multiple of $\pi/(m+1)$. Conversely Eq. (C17) only involves odd multiples.

4. High-frequency contributions: $\Lambda^{(U)}$

Here we compute the high-frequency contributions $\Lambda_{m,m'}^{(U)}(q, \tau) = \sum_x e^{iqx} \Lambda_{m,m'}^{(U)}(x, \tau)$ from adjacent regions of size m, m' to the current-current correlator. Due to the Kronecker delta on in Eq. (C8), $\Lambda_{m,m'}^{(U)}(q, \tau) = \Lambda_{m,m'}^{(U)}(\tau)$ is independent of q . This structure is seen in Fig. 6. As already introduced, we take the left segment Ω to be of length m and the right segment to be of length m' . We label the left sites as $j = -m+1, -m+2, \dots, 0$ and the right one as $i = 1, 2, \dots, m'$. Since $\Lambda_{mm'}^{(U)} = \Lambda_{m'm}^{(U)}$ there is no loss of generality in taking the right segment to be the one with heavy particles. The energy eigenstates in the left and right regions are ϕ_j^n and $\psi_i^{n'}$,

$$\phi_j^n = \sqrt{\frac{2}{m+1}} \sin k(1-j), \quad \psi_i^{n'} = \sqrt{\frac{2}{m'+1}} \sin k'i. \quad (\text{C19})$$

Here $k = \pi n/(m+1)$, $k' = \pi n'/(m'+1)$, and the eigenenergies are $v_n = -2t \cos(k)$, $\mu_{n'} = U - 2t \cos(k')$. The correlator only depends on the values of the wave functions at the boundary between the regions:

$$\phi_0^n = \sqrt{\frac{2}{m+1}} \sin k, \quad \psi_1^{n'} = \sqrt{\frac{2}{m'+1}} \sin k'. \quad (\text{C20})$$

In particular,

$$\Lambda_{m,m'}^{(U)}(\tau) = -\frac{2t^2}{m+m'} [G_{11}^>(\tau)G_{0,0}^<(-\tau) + G_{00}^>(\tau)G_{1,1}^<(-\tau)] \quad (\text{C21})$$

$$= \frac{2t^2 \bar{n}_\uparrow (1 - \bar{n}_\uparrow)}{m+m'} \sum_{n=1}^m \sum_{n'=1}^{m'} \times (e^{i(\mu_{n'} - v_n)\tau} + e^{-i(\mu_{n'} - v_n)\tau}) |\psi_1^{n'}|^2 |\phi_0^n|^2. \quad (\text{C22})$$

The full high-frequency correlator $\Lambda^{(U)}(\tau)$ can be found by inserting this result into Eq. (C11). In Fig. 1, we truncate $\Lambda^{(U)}$ at $m = m' = 20$.

-
- [1] D. J. Scalapino, S. R. White, and S. Zhang, *Phys. Rev. B* **47**, 7995 (1993).
- [2] B. Bertini, F. Heidrich-Meisner, C. Karrasch, T. Prosen, R. Steinigeweg, and M. Žnidarič, *Rev. Mod. Phys.* **93**, 025003 (2021).
- [3] E. Ilievski and J. De Nardis, *Phys. Rev. B* **96**, 081118(R) (2017).
- [4] M. Žnidarič, *Phys. Rev. Lett.* **106**, 220601 (2011).
- [5] J. De Nardis, M. Medenjak, C. Karrasch, and E. Ilievski, *Phys. Rev. Lett.* **123**, 186601 (2019).
- [6] M. Ljubotina, M. Žnidarič, and T. Prosen, *Phys. Rev. Lett.* **122**, 210602 (2019).
- [7] S. Gopalakrishnan, R. Vasseur, and B. Ware, *Proc. Natl. Acad. Sci. USA* **116**, 16250 (2019).
- [8] D. Wei, A. Rubio-Abadal, B. Ye, F. Machado, J. Kemp, K. Srakaew, S. Hollerith, J. Rui, S. Gopalakrishnan, N. Y. Yao, I. Bloch, and J. Zeiher, *Science* **376**, 716 (2022).
- [9] M. Fava, B. Ware, S. Gopalakrishnan, R. Vasseur, and S. A. Parameswaran, *Phys. Rev. B* **102**, 115121 (2020).
- [10] P. W. Anderson, *Phys. Rev.* **109**, 1492 (1958).
- [11] W. De Roeck and F. Huveneers, *Commun. Math. Phys.* **332**, 1017 (2014).
- [12] T. Grover and M. P. A. Fisher, *J. Stat. Mech.: Theory Exp.* (2014) P10010.
- [13] M. Schiulaz, A. Silva, and M. Müller, *Phys. Rev. B* **91**, 184202 (2015).
- [14] W. De Roeck and F. Huveneers, *Phys. Rev. B* **90**, 165137 (2014).

- [15] Z. Papić, E. M. Stoudenmire, and D. A. Abanin, *Ann. Phys. (NY)* **362**, 714 (2015).
- [16] N. Y. Yao, C. R. Laumann, J. I. Cirac, M. D. Lukin, and J. E. Moore, *Phys. Rev. Lett.* **117**, 240601 (2016).
- [17] J. Sirker, *Phys. Rev. B* **99**, 075162 (2019).
- [18] F. Jin, R. Steinigeweg, F. Heidrich-Meisner, K. Michielsen, and H. De Raedt, *Phys. Rev. B* **92**, 205103 (2015).
- [19] P. Zechmann, A. Bastianello, and M. Knap, *Phys. Rev. B* **106**, 075115 (2022).
- [20] N. Darkwah Oppong, G. Pasqualetti, O. Bettermann, P. Zechmann, M. Knap, I. Bloch, and S. Fölling, *Phys. Rev. X* **12**, 031026 (2022).
- [21] L. Riegger, N. Darkwah Oppong, M. Höfer, D. R. Fernandes, I. Bloch, and S. Fölling, *Phys. Rev. Lett.* **120**, 143601 (2018).
- [22] A. Heinz, A. J. Park, N. Šantič, J. Trautmann, S. G. Porsev, M. S. Safronova, I. Bloch, and S. Blatt, *Phys. Rev. Lett.* **124**, 203201 (2020).
- [23] G. Jotzu, M. Messer, F. Görg, D. Greif, R. Desbuquois, and T. Esslinger, *Phys. Rev. Lett.* **115**, 073002 (2015).
- [24] D. McKay and B. DeMarco, *New J. Phys.* **12**, 055013 (2010).
- [25] I. Bloch, J. Dalibard, and W. Zwerger, *Rev. Mod. Phys.* **80**, 885 (2008).
- [26] C. Chin, R. Grimm, P. Julienne, and E. Tiesinga, *Rev. Mod. Phys.* **82**, 1225 (2010).
- [27] W. Xu, W. McGehee, W. Morong, and B. DeMarco, *Nat. Commun.* **10**, 1588 (2019).
- [28] R. Anderson, F. Wang, P. Xu, V. Venu, S. Trotzky, F. Chevy, and J. H. Thywissen, *Phys. Rev. Lett.* **122**, 153602 (2019).
- [29] P. T. Brown, D. Mitra, E. Guardado-Sanchez, R. Nourafkan, A. Reymbaut, C.-D. Hébert, S. Bergeron, A.-M. S. Tremblay, J. Kokalj, D. A. Huse, P. Schauß, and W. S. Bakr, *Science* **363**, 379 (2019).
- [30] C. Gross and I. Bloch, *Science* **357**, 995 (2017).
- [31] E. H. Lieb and F. Y. Wu, *Phys. Rev. Lett.* **20**, 1445 (1968).
- [32] H. J. Schulz, *Phys. Rev. Lett.* **64**, 2831 (1990).
- [33] L. M. Falicov and J. C. Kimball, *Phys. Rev. Lett.* **22**, 997 (1969).
- [34] T. Heitmann, J. Richter, T. Dahm, and R. Steinigeweg, *Phys. Rev. B* **102**, 045137 (2020).
- [35] R. Kubo, *J. Phys. Soc. Jpn.* **12**, 570 (1957).
- [36] N. H. Lindner and A. Auerbach, *Phys. Rev. B* **81**, 054512 (2010).
- [37] E. Perepelitsky, A. Galatas, J. Mravlje, R. Žitko, E. Khatami, B. S. Shastry, and A. Georges, *Phys. Rev. B* **94**, 235115 (2016).
- [38] T. G. Kiely and E. J. Mueller, *Phys. Rev. B* **104**, 165143 (2021).
- [39] A. A. Patel and H. J. Changlani, *Phys. Rev. B* **105**, L201108 (2022).
- [40] U. Schollwöck, *Ann. Phys. (NY)* **326**, 96 (2011).
- [41] S. Paeckel, T. Köhler, A. Swoboda, S. R. Manmana, U. Schollwöck, and C. Hubig, *Ann. Phys. (NY)* **411**, 167998 (2019).
- [42] D. Kennes and C. Karrasch, *Comput. Phys. Commun.* **200**, 37 (2016).
- [43] T. G. Kiely and E. J. Mueller, *Phys. Rev. B* **106**, 235126 (2022).
- [44] H. N. Phien, G. Vidal, and I. P. McCulloch, *Phys. Rev. B* **88**, 035103 (2013).
- [45] A. Milsted, J. Haegeman, T. J. Osborne, and F. Verstraete, *Phys. Rev. B* **88**, 155116 (2013).
- [46] V. Zauner, M. Ganahl, H. G. Evertz, and T. Nishino, *J. Phys.: Condens. Matter* **27**, 425602 (2015).
- [47] M. P. Zaletel, R. S. K. Mong, C. Karrasch, J. E. Moore, and F. Pollmann, *Phys. Rev. B* **91**, 165112 (2015).
- [48] M. Yang and S. R. White, *Phys. Rev. B* **102**, 094315 (2020).
- [49] E. Guardado-Sanchez, A. Morningstar, B. M. Spar, P. T. Brown, D. A. Huse, and W. S. Bakr, *Phys. Rev. X* **10**, 011042 (2020).
- [50] J. Haegeman, J. I. Cirac, T. J. Osborne, I. Pivzorn, H. Verschelde, and F. Verstraete, *Phys. Rev. Lett.* **107**, 070601 (2011).
- [51] C. D. White, M. Zaletel, R. S. K. Mong, and G. Refael, *Phys. Rev. B* **97**, 035127 (2018).
- [52] T. Rakovszky, C. W. von Keyserlingk, and F. Pollmann, *Phys. Rev. B* **105**, 075131 (2022).
- [53] S. N. Thomas, B. Ware, J. D. Sau, and C. D. White, *arXiv:2310.06886*.
- [54] H. Kim and D. A. Huse, *Phys. Rev. Lett.* **111**, 127205 (2013).
- [55] M. Dupont and J. E. Moore, *Phys. Rev. B* **101**, 121106(R) (2020).